

See discussions, stats, and author profiles for this publication at: <https://www.researchgate.net/publication/255787308>

# One-Step, Surfactant-Free Hydrothermal Method for Syntheses of Mesoporous TiO<sub>2</sub> Nanoparticle Aggregates and Their Applications in High Efficiency Dye-Sensitized Solar Cells

**DATASET** in CHEMISTRY OF MATERIALS · JULY 2012

Impact Factor: 8.35 · DOI: 10.1021/cm3017616

---

CITATIONS

31

---

READS

75

## 5 AUTHORS, INCLUDING:



Juti Rani Deka

National Central University

29 PUBLICATIONS 167 CITATIONS

[SEE PROFILE](#)



Shih-Yuan Lu

National Tsing Hua University

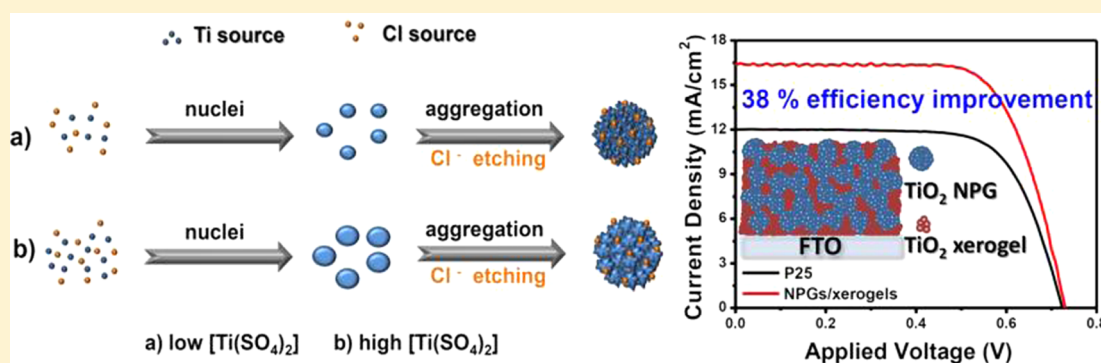
157 PUBLICATIONS 3,014 CITATIONS

[SEE PROFILE](#)

# One-Step, Surfactant-Free Hydrothermal Method for Syntheses of Mesoporous $\text{TiO}_2$ Nanoparticle Aggregates and Their Applications in High Efficiency Dye-Sensitized Solar Cells

Wei-Yun Cheng, Juti Rani Deka, Yi-Chun Chiang, Antoine Rogeau, and Shih-Yuan Lu\*

Department of Chemical Engineering, National Tsing-Hua University, Hsinchu 30013, Taiwan



**ABSTRACT:** A facile, one-step, template-less, surfactant-free hydrothermal process, using a metal salt as the precursor, is developed to prepare submicrometer sized mesoporous  $\text{TiO}_2$  nanoparticle aggregates (NPGs). The as-prepared  $\text{TiO}_2$  NPGs are crystalline of the anatase phase, with a high specific surface area of  $166 \text{ m}^2/\text{g}$ , an average pore size of  $8.9 \text{ nm}$ , and an average NPG size of  $840 \text{ nm}$ . With these NPGs, a new form of composite photoanode, consisting of the mesoporous  $\text{TiO}_2$  NPGs and xerogels, is proposed for high efficiency dye-sensitized solar cells (DSSCs).  $\text{TiO}_2$  xerogels are incorporated into the  $\text{TiO}_2$  NPGs layer with an impregnation process to form the  $\text{TiO}_2$  NPGs/xerogels composite. A high power conversion efficiency of  $8.41\%$  is achieved for DSSCs based on the  $\text{TiO}_2$  NPGs/xerogels composite photoanode, representing a  $38\%$  efficiency boost over the efficiency of  $6.11\%$  achieved with a P25  $\text{TiO}_2$  based cell. The success of the present composite  $\text{TiO}_2$  nanostructure can be attributed to the effective utilization of the inter-NPG space with the infiltration of the  $\text{TiO}_2$  xerogels, the excellent structural connectivity within and across the NPG and xerogel domains for fast electron transport, the high specific surface areas of both the NPGs and xerogels for providing abundant dye adsorption for generation of photoinduced electrons, the formation of a  $\text{TiO}_2$  xerogel blocking layer on top of the photoanode substrate, and the submicrometer size of the NPGs for much improved light harvesting efficiency. This new type of composite photoanode, different from the 0D/1D nanostructure based ones, proves effective by taking structural advantages from both constituent nanostructures, the mesoporous NPGs and xerogels, and opens up a new way of thinking in the structural design of the photoanodes.

**KEYWORDS:** mesoporous nanoparticle aggregate, hydrothermal, dye-sensitized solar cell, xerogel, composite photoanode

## 1. INTRODUCTION

Dye sensitized solar cells (DSSC), because of their excellent performance to cost ratios, remain as one of the promising alternative clean energy harvesting technologies and continue to draw a great deal of research attention.<sup>1–5</sup> A DSSC is basically composed of a photoanode, a catalytic counter electrode, and an electrolyte solution. The photoanode is often constructed by casting a dye-sensitized, mesoporous, nanocrystalline semiconductor film on a transparent conductive glass, to absorb and convert photons to electrons and to transport and collect the photoinduced electrons. The catalytic counter electrode acts as the cathode to regenerate electrolyte ions of reduced state. And an iodide/tri-iodide redox couple dissolved in a proper mediator is commonly used as the electrolyte to regenerate ground state dye molecules and to transport tri-iodide ions to the counter electrode.<sup>1,3</sup> To further

boost the power conversion efficiency of the cell, intensive and extensive research efforts have been made on all relevant aspects of the DSSCs, including photoanodes, dyes, electrolytes, and counter electrodes.<sup>6–10</sup> In particular, the transport of electrons across the photoanode layer has been identified as the bottleneck of the whole charge transport loop of the DSSCs.<sup>11</sup> Consequently, a great deal of research attention has been paid to the development of novel nanostructure for photoanodes in an attempt to speed up the electron transport across the photoanode layer without being consumed by the back electron transfer reactions. In this regard, one-dimensional (1D) nanostructures, including nanowires,<sup>12,13</sup> nanorods,<sup>14,15</sup> nano-

Received: June 7, 2012

Revised: July 24, 2012

Published: July 29, 2012

tubes,<sup>16,17</sup> and even elongated nanoparticles,<sup>18</sup> have been utilized in photoanode fabrication, mainly targeting for enhanced charge transport along the confined and often single-crystalline one-dimensional pathways. Plain 1D nanostructure based photoanodes, however, failed to improve the power conversion efficiency of the cell, mainly because of the lack of necessary large surface areas for dye adsorption, although enhanced charge transport was indeed achieved accompanied with enhanced light harvesting resulting from the intense light scattering offered by the much longer characteristic lengths in the axial direction of the 1D nanostructure.

For photoanodes, the generation of photoinduced electrons is also essential in addition to charge transport. To achieve this functional goal, two structural features of the photoanodes are desirable: large specific surface areas and excellent light scattering ability. The former is required to acquire high dye loadings and subsequent generation of photoinduced electrons. The latter helps to utilize the incoming light to a fuller extent for light absorption by the dye molecules and following generation of photoinduced electrons and can be achieved by introducing structures of submicrometers into the photoanode layer or by overlaying a light scattering layer of submicrometer  $\text{TiO}_2$  particles.<sup>19–21</sup> To simultaneously satisfy the two essential requirements of the photoanode, namely, the abundant generation of photoinduced electrons and fast electron transport, the concept of composite photoanodes, composed of 0D nanoparticles and 1D nanostructure, was proposed, with the 0D nanoparticles supplying large surface areas while 1D nanostructures offered fast electron transport pathways and enhanced light scattering.<sup>7,21,23</sup> At some optimum combinations of the two nanostructures, the power conversion efficiencies were significantly improved.

In addition to the composite photoanode concept, the idea of creating a nanostructure that offers not only large surface areas but also excellent light scattering ability was proposed. This idea was realized with mesoporous nanoparticle aggregates (NPG) of submicrometer sizes, from which the structural preference of large surface areas and excellent light scattering can be simultaneously achieved.<sup>24–26</sup> Furthermore, the well-connected, chemically bonded constituent nanocrystals of the NPGs offer continuous pathways for the transport of the photoinduced electrons within the NPGs. With all the important aspects of the photoanode fulfilled, the mesoporous  $\text{TiO}_2$  NPGs based photoanodes led to impressive high power conversion efficiencies of the cells.

In this work, we propose a new form of composite photoanodes that combines the advantages of composite nanostructure with mesoporous  $\text{TiO}_2$  NPGs. The idea is to remove some drawbacks associated with the plain NPGs based photoanodes, such as the waste of the inter-NPG space and the poor connections between the submicrometer sized NPGs. We propose to fill up the inter-NPG space with mesoporous  $\text{TiO}_2$  xerogels. Xerogels are a class of mesoporous materials possessing high specific surface areas and porosities, constructed by three-dimensional networks of well-connected constituent nanoparticles.<sup>27–29</sup> The  $\text{TiO}_2$  xerogels can not only fill up the inter-NPG space to supply more surfaces for dye adsorption but also connect the NPGs together to offer ample, continuous inter-NPG communication pathways. Furthermore, the infiltrated  $\text{TiO}_2$  xerogels can form a blocking layer on top of the photoanode substrate to suppress possible recombination of electrons reaching the substrate, with oxidized dye molecules

or electrolyte ions. Consequently, the infiltration of the  $\text{TiO}_2$  xerogel can also fulfill the functions conventionally served by  $\text{TiO}_2$  blocking layers and  $\text{TiCl}_4$  treatments.

The preparation of the mesoporous  $\text{TiO}_2$  NPGs in the past requires a two-step process, sol–gel followed by solvothermal, and structure-directing reagents are involved in the process.<sup>30–33</sup> In this work, we develop a facile one-step hydrothermal process to prepare the mesoporous  $\text{TiO}_2$  NPGs without the involvement of soft molecular templates resulting from surfactants. In addition, a metal salt is used as the precursor. The as-prepared  $\text{TiO}_2$  NPGs from the present process are crystalline with the preferred anatase phase and are mesoporous with a high specific surface area of  $166 \text{ m}^2/\text{g}$  and an average pore size of  $8.9 \text{ nm}$ . These characteristics are favorable for the applications in DSSCs as the photoanode. The present process for the mesoporous  $\text{TiO}_2$  NPG production is scalable and promising for commercial applications in DSSCs.

The composite photoanode proposed in this work leads to a 38% improvement in the power conversion efficiency over the P25  $\text{TiO}_2$  based DSSCs. The success is attributed to the structural advantages of the composite photoanode, realized by the combination of the mesoporous  $\text{TiO}_2$  NPGs and xerogels.

## 2. EXPERIMENTAL SECTION

**2.1. Synthesis of Mesoporous  $\text{TiO}_2$  NPGs.** The mesoporous  $\text{TiO}_2$  NPGs are produced via a one-step hydrothermal process. Typically,  $0.267 \text{ g}$  of ammonium chloride and  $80 \text{ mL}$  of deionized (DI) water are added into an autoclave of a capacity of  $100 \text{ mL}$ . The mixture is stirred to complete dissolution. One gram of titanium sulfate solution (24%, Kanto Chemical) is then mixed with the above solution and sealed in a stainless steel container for a hydrothermal treatment at  $200^\circ\text{C}$  for  $12 \text{ h}$ . After the hydrothermal treatment, the precipitates are collected and rinsed with DI water twice and ethanol once by ultrasonication and centrifuge before being dried in an oven of  $80^\circ\text{C}$  to afford the mesoporous  $\text{TiO}_2$  NPGs.

**2.2. Preparation of Photoanodes. Plain  $\text{TiO}_2$  NPGs or P25  $\text{TiO}_2$  Based Photoanode.** The photoanode is fabricated by doctor-blade casting a film of NPGs or P25 paste onto a fluorine doped tin oxide (FTO) glass. The pastes are prepared by mixing  $0.2 \text{ g}$  of NPGs or P25 powders with a binder solution composed of  $0.025 \text{ g}$  of ethyl cellulose (200 cps, Showa) and  $1 \text{ mL}$  of  $\alpha$ -terpineol (95%, Showa). The as-fabricated photoanodes, after being dried at  $100^\circ\text{C}$  with a hot plate for  $20 \text{ min}$ , are calcined at  $450^\circ\text{C}$  for  $30 \text{ min}$  to remove the residual solvent and binder and also to enhance the adhesion between the NPGs or P25 powders and the FTO glass.

**$\text{TiO}_2$  NPGs/Xerogels Composite Based Photoanode.** If the  $\text{TiCl}_4$  treatment is to be conducted, the as-fabricated photoanodes are immersed into a  $0.2 \text{ M}$  ethanolic solution of  $\text{TiCl}_4$  at  $80^\circ\text{C}$  for  $30 \text{ min}$  followed by rinsing with DI water to form  $\text{TiO}_2$  nanoparticles on the surface of the primitive  $\text{TiO}_2$  nanostructure. After room temperature drying in air, the product is further calcined at  $450^\circ\text{C}$  for  $2 \text{ h}$  to acquire the crystallinity of the newly generated  $\text{TiO}_2$  nanoparticles. As for the fabrication of the  $\text{TiO}_2$  NPGs/xerogels composite photoanode, the procedure is as follows. First,  $3.025 \text{ mL}$  titanium isopropoxide is added into  $2.575 \text{ mL}$  ethanol to form solution A. Next,  $0.0554 \text{ mL}$  nitric acid and  $0.34 \text{ mL}$  DI water are mixed with  $7.715 \text{ mL}$  ethanol to form solution B. The two solutions are then mixed and stirred to afford a clear solution of  $\text{TiO}_2$  sols. The plain  $\text{TiO}_2$  NPGs based photoanodes are soaked in the above sol solution for  $1 \text{ h}$  before being transferred to a closed vessel to age the sols for three days for formation of the gel within the NPGs layer. After the gelation, the photoanodes are dried at room temperature followed by calcination at  $450^\circ\text{C}$  for  $2 \text{ h}$  to afford the  $\text{TiO}_2$  NPGs/xerogels composite based photoanodes. The thicknesses of all photoanodes, including P25 and NPGs based ones, are controlled to be  $12 \mu\text{m}$  for the DSSC assembly.

**2.3. Characterizations of Mesoporous  $\text{TiO}_2$  NPGs.** A field-emission scanning electron microscope (FESEM, Hitachi S-4700) is

used to observe the morphology of the  $\text{TiO}_2$  NPGs and fabricated photoanodes and to determine the thicknesses of the photoanodes. An X-ray powder diffractometer (XRD, MAC Science MXP 18) is used to determine the crystalline phase, grain size, and phase purity of the  $\text{TiO}_2$  NPGs. The crystallographic structure of the samples is further investigated with a high-resolution transmission electron microscope (HRTEM, JEOL JEM-3000) and an analytic transmission electron microscope (AEM, JEOL JEM-2010). The microstructural characteristics of the samples are measured with the  $\text{N}_2$  adsorption/desorption analyses conducted at 77 K (Quantachrome, NOVA e1000). A UV-visible spectrophotometer (Hitachi, U-3300) is used to measure the transmittances of the fabricated photoanodes.

**2.4. Fabrication and Performances of DSSCs.** The photoanodes with a working area of  $0.25 \text{ cm}^2$  are heated at  $120^\circ\text{C}$  for 10 min to remove the trapped air and moisture. They are then soaked in a  $0.3 \text{ mM}$  *cis*-bis(isothiocyanato)bis(2,2'-bipyridi-4,4'-dicarboxylatoruthenium(II)bis-tetrabutylammonium (N719, Solaronix) solution for 12 h for dye adsorption. Here the solvent for the N719 dye is composed of ethanol and acetonitrile at a volume ratio of 1:1. As for the electrolyte, acetonitrile is used as the solvent and the electrolyte contains  $0.6 \text{ M}$  1-propyl-2,3-dimethylimidazolium iodide (99%, Aldrich),  $0.1 \text{ M}$  lithium iodide (99.9%, Aldrich),  $0.05 \text{ M}$  iodine (99.5%, Fluka), and  $0.6 \text{ M}$  *tert*-butyl pyridine (98%, Fluka). A  $50 \text{ nm}$  thick Pt film is deposited onto a silicon wafer with sputtering and serves as the counter electrode for the cell. To fabricate the cell, a spacer with a thickness of  $25 \mu\text{m}$  is used to connect the counter electrode and photoanode. The current density–voltage ( $J$ – $V$ ) curves of the cells are recorded with a source meter (Kiethley 236, Kiethley) under illumination of a solar simulator (Yamashita Denso, YSS-E40; AM 1.5,  $100 \text{ mW cm}^{-2}$ ) calibrated by a reference Si solar cell (SN2008-152, Yamashita). The incident photon to charge carrier efficiency (IPCE, ENLI, EQE-D-3011), electrochemical impedance spectroscopy (EIS, AUTOLAB PGSTAT30), and intensity-modulated photovoltage/photocurrent spectroscopy (IMVS/IMPS, AUTOLAB PGSTAT30) are conducted to analyze the charge transport characteristics of the photoanodes. The IMVS and IMPS are equipped with a blue light laser diode of a wavelength of  $470 \text{ nm}$  as the light source, driven by a Dyload interface that is connected to an AUTOLAB instrument (PGSTAT30) as the frequency response analyzer. The frequency is scanned from  $10^5$  to  $0.1 \text{ Hz}$ .

### 3. RESULTS AND DISCUSSION

There are only two chemicals involved in the preparation of the mesoporous  $\text{TiO}_2$  NPGs, namely,  $\text{Ti}(\text{SO}_4)_2$  and  $\text{NH}_4\text{Cl}$ . Here,  $\text{Ti}(\text{SO}_4)_2$  is the Ti source and  $\text{NH}_4\text{Cl}$  provides chloride ions mainly for the structure etching and possibly structure directing purposes. We first investigate how the molar concentration of  $\text{Ti}(\text{SO}_4)_2$ ,  $[\text{Ti}(\text{SO}_4)_2]$ , and the molar ratio of the two chemicals,  $R = [\text{NH}_4\text{Cl}]/[\text{Ti}(\text{SO}_4)_2]$ , affect the microstructural characteristics of the products, including specific surface areas, average pore sizes, and grain sizes. The results are summarized in Table 1.

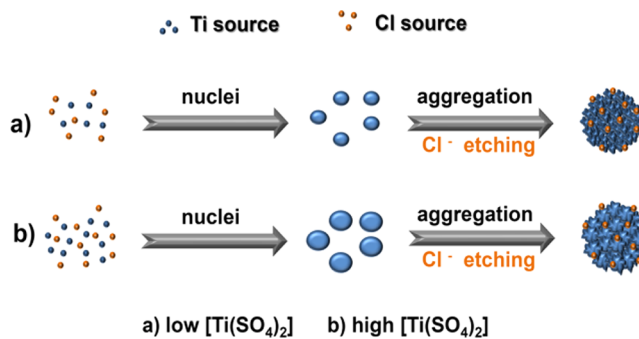
When the molar ratio is fixed, the specific surface area of the product NPGs decreases with increasing molar concentration of the Ti source. This can be understood by considering the formation mechanism of the NPGs as illustrated in Scheme 1. The  $\text{TiO}_2$  nuclei are formed first from the hydrolysis, condensation, and polymerization of the Ti source. These nuclei then grow to larger nanocrystals of sizes around  $10 \text{ nm}$ , depending on the supply of the Ti source. Higher (lower) molar concentrations of the Ti source lead to larger (smaller) nanocrystals. The mesoporous  $\text{TiO}_2$  NPGs are finally formed through aggregation of the constituent nanocrystals accompanied by internanocrystal growth and etching of the NPGs with chloride ion. Note that, in the absence of  $\text{NH}_4\text{Cl}$ , the specific surface area and average pore size of the product are  $177 \text{ m}^2/\text{g}$  and  $5.1 \text{ nm}$ , respectively. Although the specific

**Table 1. Reaction Conditions and Microstructural Parameters of the Product  $\text{TiO}_2$  NPGs**

$[\text{Ti}(\text{SO}_4)_2]$ [M]	R	specific surface area <sup>a</sup> [ $\text{m}^2/\text{g}$ ]	avg. pore size <sup>a</sup> [nm]	grain size <sup>b</sup> [nm]
0.1	3	87	11.6	16.3
0.05	3	115	9.0	14.8
0.03	3	136	8.8	10.6
0.0125	1	173	4.6	9.1
0.0125	3	155	9.1	8.8
0.0125	5	166	8.9	8.4

<sup>a</sup>Specific surface areas and average pore sizes were calculated based on the BET and BJH models, respectively. <sup>b</sup>Grain sizes were determined from the Scherrer equation based on the diffraction peak (101).

**Scheme 1. Mechanism for NPG Formation**



surface area is the highest among all samples, this product is not NPGs and has a structure of not well-defined shape with a characteristic size larger than at least  $1 \mu\text{m}$ . More importantly, the average pore size is too small to be favorable for the photoanode application. The average pore size of the mesoporous NPGs decreases and levels off with decreasing molar concentration of  $\text{Ti}(\text{SO}_4)_2$ . The grain size, as estimated from the XRD patterns with the Scherrer equation based on the diffraction peak (101), also decreases with decreasing  $[\text{Ti}(\text{SO}_4)_2]$ . The sizes of the constituent nanocrystals as estimated from the SEM images are approximately equal to those of the corresponding grain sizes, implying the single crystalline nature of the constituent nanocrystals. Therefore, the trend we observed for the grain size of the NPGs is consistent with the specific surface area data, smaller constituent nanocrystal sizes corresponding to larger specific surface areas.

The effect of the molar ratio does not seem to be significant, only that, at the low molar ratio of 1, corresponding to a low  $\text{NH}_4\text{Cl}$  concentration, the average pore size is relatively small, which may be because of the insufficient etching of the NPG structure by the chloride ions. Interestingly, no  $\text{TiO}_2$  NPGs can be formed when the R value is lower than 1. Although the specific surface area of the NPGs is the highest at  $173 \text{ m}^2/\text{g}$  for the reaction condition of  $[\text{Ti}(\text{SO}_4)_2] = 0.0125 \text{ M}$  and  $R = 1$ , the corresponding average pore size of  $4.6 \text{ nm}$  may present a large internal mass transfer resistance within the NPGs and hinder the photon to electron conversion of the cell. We thus use the product NPGs obtained at the reaction condition of  $[\text{Ti}(\text{SO}_4)_2] = 0.0125 \text{ M}$  and  $R = 5$  for the subsequent study.

Figure 1a shows the SEM image of typical  $\text{TiO}_2$  NPGs. These NPGs are mostly granular in shape, although some of them are in dumbbell or even more elongated shape, and are with an average NPG size of around  $840 \pm 105 \text{ nm}$ . The aggregate size was defined as the arithmetic average of the long

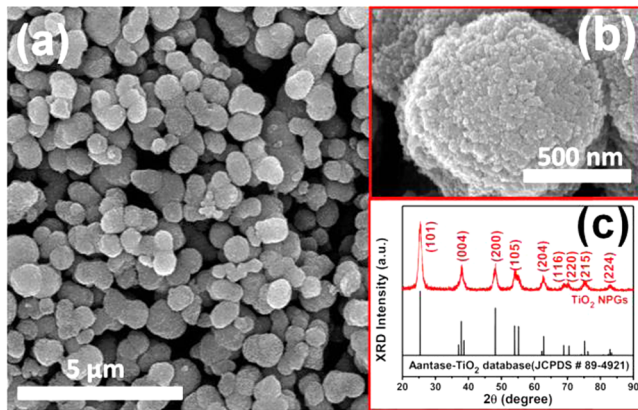


**Figure 1.** SEM images of  $\text{TiO}_2$  NPGs at (a) low and (b) high magnifications. (c) XRD pattern of as-prepared  $\text{TiO}_2$  NPGs.

and short axes of the aggregate, and the average aggregate size and standard deviation were obtained based on SEM images of 25 NPGs. This submicrometer size is favorable for offering intense light scattering for enhanced light harvesting of the cell. From the high magnification SEM image of Figure 1b, the NPGs are evidently composed of nanoparticles of around 10 nm in size. These nanoparticles are strongly connected together with one another and cannot be broken apart even under strong ultrasonication. Mesopores are formed within the NPGs because of the aggregation of the nanoparticles and also the etching of the NPGs with the chloride ions. The as-prepared  $\text{TiO}_2$  NPGs are with good crystallinity of the anatase phase as can be seen from the well-resolved diffraction peaks and the perfect matching of the diffraction pattern with the database pattern of JCPDS no. 89-4921. The grain size of 8.4 nm can be readily determined from the Scherrer equation. The closeness between the grain size and the nanoparticle size implies that the constituent nanoparticles are in fact single crystalline, which is beneficial for fast charge transport.

The microstructure of the product NPGs is further examined with TEM as shown in Figure 2. The low magnification TEM image of Figure 2a shows again the predominantly granular shape of the NPGs and their submicrometer average sizes. If examined closely, the edge of the NPGs, where the thickness is small enough for the electron beams to penetrate through, can be observed to be porous in morphology. This can be more

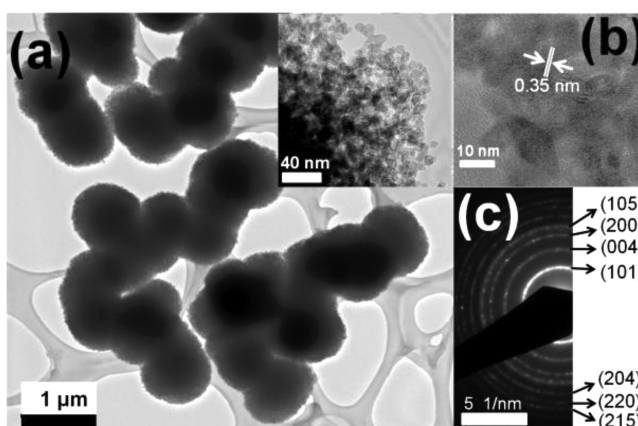


**Figure 2.** (a) TEM, (b) high resolution TEM images, and (c) selected-area electron diffraction pattern of  $\text{TiO}_2$  NPGs.

clearly seen from the inset of Figure 2a, which is a local enlargement of a typical NPG.

Figure 2b is an HRTEM image revealing the detailed microstructure and crystallographic structure of a NPG. Mesopores can be identified from the image, and an interlayer spacing of 0.35 nm is determined from the lattice fringes, in good agreement with the  $d$ -spacing of the (101) planes of anatase  $\text{TiO}_2$ . The sizes of the constituent nanocrystals are around 10 nm, consistent with the grain size estimated from the XRD pattern. Figure 2c shows the selected-area electron diffraction (SAED) pattern of the NPGs. The resulting ring pattern indicates the polycrystallinity of the NPGs and the rings can be assigned to the (101), (004), (200), (105), (204), (220), and (215) planes of the anatase  $\text{TiO}_2$ , complying with the results of the XRD analyses.

The microstructural characteristics of the NPGs are further investigated with the  $\text{N}_2$  adsorption/desorption analysis. A typical result is shown in Figure 3. Figure 3 exhibits a type IV

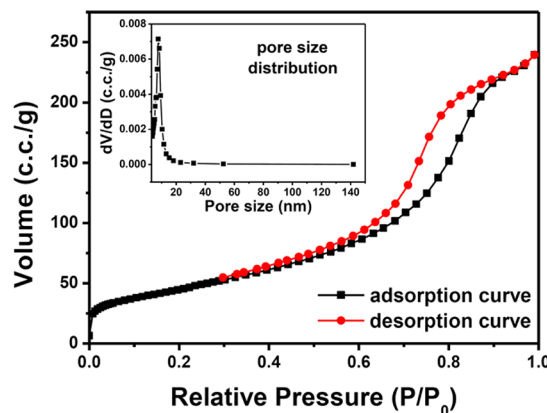


**Figure 3.**  $\text{N}_2$  adsorption/desorption curve of  $\text{TiO}_2$  NPGs. Inset is pore size distribution of  $\text{TiO}_2$  NPGs.

isotherm with a clear type H3 hysteresis, typical for mesoporous materials. The specific surface area is determined from the isotherms to be  $166 \text{ m}^2/\text{g}$  based on the BET model. The pore size distribution is depicted as an inset of Figure 3. Evidently, the sizes of most of the pores concentrate between 5 and 10 nm, with an average pore size of 8.9 nm estimated with the BJH method. The high specific surface area is desirable for dye adsorption, and the average pore size of 8.9 nm is adequate for penetration of the dye molecules into the NPGs and mass transfer of the electrolyte ions in and out of the NPGs.

The product  $\text{TiO}_2$  NPGs are cast onto FTO glass to serve as the photoanode of the DSSCs. In Figure 4, we examine the morphology and light transmittance of the resulting photoanodes. Figure 4a–c shows the cross sectional FESEM images of three different  $\text{TiO}_2$  NPGs based photoanodes, plain  $\text{TiO}_2$  NPGs, plain  $\text{TiO}_2$  NPGs after  $\text{TiCl}_4$  treatment, and  $\text{TiO}_2$  NPGs/xerogels composite, respectively. The upper right insets of Figure 4a–c are the corresponding top view FESEM images of the photoanodes.

For the plain  $\text{TiO}_2$  NPGs based photoanode, there can be observed abundant voids between NPGs, which can also be concluded from the top view FESEM image of the photoanode, with ample inter-NPG space clearly visible. After the  $\text{TiCl}_4$  treatment, the introduced  $\text{TiO}_2$  nanoparticles can only cover the surfaces of the structure and fill the local space around the NPG junctions to improve the connection between par-

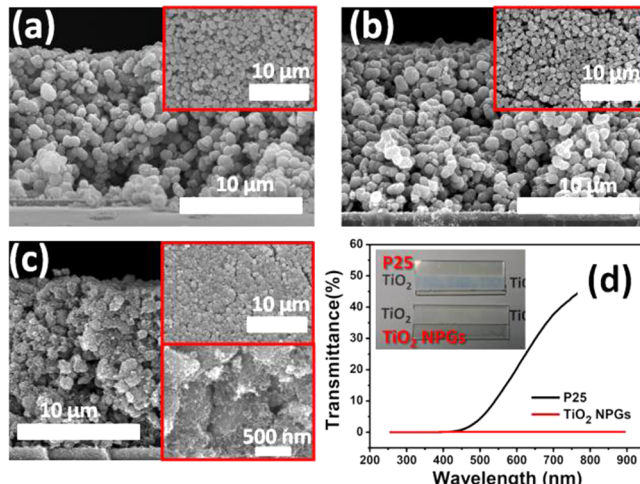


**Figure 4.** Cross-sectional view FESEM images of cast layers of (a) TiO<sub>2</sub> NPGs, (b) TiO<sub>2</sub> NPGs/TiCl<sub>4</sub> treatment, and (c) TiO<sub>2</sub> NPGs/xerogels. Insets are corresponding top view FESEM images. The lower right inset of (c) is a local enlargement of the cross-sectional image. (d) Transmittance spectra of P25 TiO<sub>2</sub> and TiO<sub>2</sub> NPGs based photoanodes. Inset is a picture for the two samples.

ticles<sup>6,30,34</sup> but cannot form 3D structure to fill up the inter-NPG space. At the magnification level used for Figure 4b, the morphology of the photoanode appears almost the same with that of the plain TiO<sub>2</sub> NPGs based photoanode. As for the TiO<sub>2</sub> NPGs/xerogels composite photoanode, evident morphological differences can be observed as shown in Figure 4c. Such morphological differences exist across the whole photoanode layer, implying a thorough impregnation of the photoanode layer with the TiO<sub>2</sub> sols. After gelation and drying, the TiO<sub>2</sub> sols form a 3D network filling up the inter-NPG space and connecting the separate NPGs together. If examined closely, one can even observe the remaining 3D network from the lower right inset of Figure 4c, even though most of them are destroyed at the cleaving stage of the sample preparation. The inter-NPG filling can be clearly identified from the top view FESEM image of the upper right inset of Figure 4c, in which the inter-NPG space almost disappears. It is worth mentioning that the overgrown xerogel layer can be easily peeled off after drying. The filling up of the inter-NPG space with TiO<sub>2</sub> xerogels and improved inter-NPG connection are beneficial for dye adsorption and charge transport within the photoanode. To investigate the light scattering effect of the TiO<sub>2</sub> NPGs for the photoanode, we compare the transmittance spectra of two photoanodes in Figure 4d, one P25 TiO<sub>2</sub> based and the other TiO<sub>2</sub> NPGs based, both at a thickness of 12 μm. For the former, the transmittance increases with increasing wavelength from 400 to 800 nm and reaches a maximum value of about 45% at 800 nm. On the contrary, because of the intense light scattering offered by the submicrometer size of the TiO<sub>2</sub> NPGs, almost no light of the tested wavelength range can penetrate through the TiO<sub>2</sub> NPGs layer. The inset picture displayed in Figure 4d shows the actual appearances of the two photoanodes. The photoanodes are placed above a sheet with two parallel lines of “TiO<sub>2</sub>” written. For the P25 sample, the “TiO<sub>2</sub>” words beneath the photoanode can still be vaguely identified, whereas for the TiO<sub>2</sub> NPGs sample the “TiO<sub>2</sub>” words are completely obscured because of the intense light scattering effect of the TiO<sub>2</sub> NPGs. It is worth noting that the TiO<sub>2</sub> NPG and TiO<sub>2</sub> xerogels, although both mesoporous, differ in

porosities. The TiO<sub>2</sub> NPG is denser than TiO<sub>2</sub> xerogel. Consequently, they can be viewed as two different domains of different effective refractive indices, from which light scattering occurs. Also note that these two domains are porous, not dense, in structure and there are void spaces available for light scattering to work.

The performances of the TiO<sub>2</sub> NPGs as a photoanode material are investigated by measuring the current density vs applied voltage (*J*-*V*) curves of the DSSCs constructed based on the NPGs. Included in the performance comparison are four different photoanodes, P25, TiO<sub>2</sub> NPGs, TiO<sub>2</sub> NPGs/TiCl<sub>4</sub> treatment, and TiO<sub>2</sub> NPGs/xerogels based ones. The resulting *J*-*V* curves are shown in Figure 5a with the important

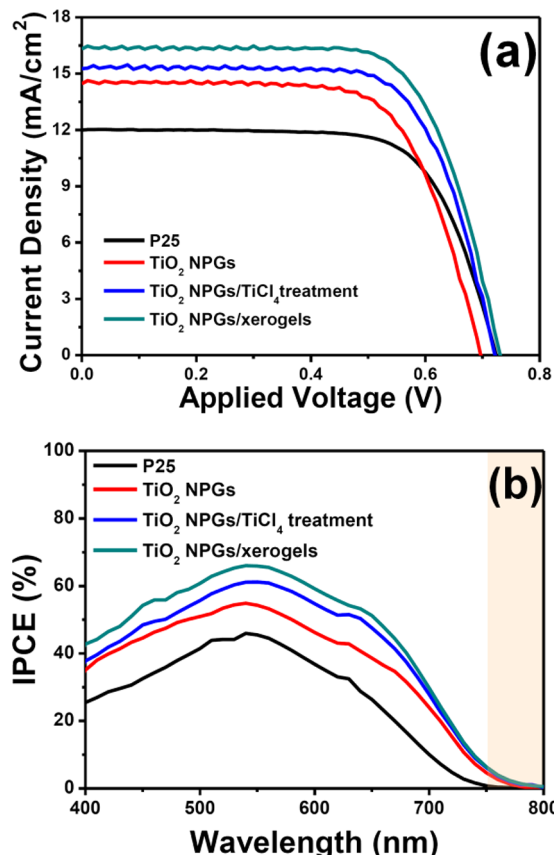


**Figure 5.** (a) *J*-*V* curves and (b) IPCE spectra of P25, TiO<sub>2</sub> NPGs, TiO<sub>2</sub> NPGs/TiCl<sub>4</sub> treatment and TiO<sub>2</sub> NPGs/xerogels based cells.

performance indices summarized in Table 2, including the open circuit voltage (*V*<sub>oc</sub>), short circuit current density (*J*<sub>sc</sub>), fill factor

**Table 2. Open Circuit Voltage, Short Circuit Current Density, Fill Factor, Power Conversion Efficiency, and Dye Loading of P25, TiO<sub>2</sub> NPGs, TiO<sub>2</sub> NPGs/TiCl<sub>4</sub> treatment, and TiO<sub>2</sub> NPGs/Xerogels Based Cells**

	<i>V</i> <sub>oc</sub> [V]	<i>J</i> <sub>sc</sub> [mA/cm <sup>2</sup> ]	FF	<i>η</i> [%]	dye loading [10 <sup>-7</sup> mol/cm <sup>2</sup> ]
P25	0.72	12.0	0.7	6.11	0.71
TiO <sub>2</sub> NPGs	0.69	14.4	0.69	6.92	1.15
TiO <sub>2</sub> NPGs/ TiCl <sub>4</sub>	0.72	15.3	0.7	7.77	1.27
TiO <sub>2</sub> NPGs/ xerogels	0.73	16.3	0.7	8.41	1.36

(FF), power conversion efficiency ( $\eta$ ), and dye loading. There are several points worth discussion. First, the  $V_{oc}$  of the  $TiO_2$  NPGs based cell is non-negligibly lower than that of the P25 based cell. This may be understood as the significantly poorer contact of the micrometer-sized NPGs with the FTO substrate than that achieved by the nanosized P25  $TiO_2$  particles. After the  $TiCl_4$  treatment, a thin layer of  $TiO_2$  nanoparticles is generated to cover the surface of the FTO substrate for prevention of the photoinduced electrons reaching the substrate to recombine with the oxidized dye molecules or electrolyte ions. Furthermore, the  $TiCl_4$  treatment can improve the connectivity between  $TiO_2$  NPGs for better charge transport. Consequently, an appreciable improvement in  $V_{oc}$  is achieved. As for the  $TiO_2$  NPGs/xerogels based cell, the xerogels not only fill up the inter-NPG space but also form a thin layer on top of the substrate as the  $TiCl_4$  treatment does. The 3D network structure of the xerogels provides a much improved charge transport between the NPGs and thus further boosts the  $V_{oc}$  to 0.73 V.

In addition to the improvement in  $V_{oc}$ , the  $TiO_2$  NPGs/xerogels composite photoanode can achieve much more drastic and important enhancement in dye loading,  $J_{sc}$  and thus the power conversion efficiency. The dye loading basically increases with increasing surface area of the photoanode. The P25  $TiO_2$  possesses a specific surface area of 50  $m^2/g$ , which is much lower than 166  $m^2/g$  of the  $TiO_2$  NPGs. The  $TiCl_4$  treatment on the  $TiO_2$  NPGs increases the specific surface area of the NPGs, but in a lesser extent as compared with the incorporation of  $TiO_2$  xerogels. Consequently, one observes the increasing trend in dye loading as shown in the last column of Table 2. The amount of dye adsorption directly correlates with the amount of photoinduced electrons created within the photoanode under light illumination. Furthermore, the light scattering of the photoanode also contributes significantly to the generation of photoinduced electrons as the light utilization is enhanced. In addition, the improved inter-NPG connectivity through the filling of the xerogels facilitates the charge transport across the NPGs. With all these factors taken into account, one obtains the increasing trends in  $J_{sc}$  and thus  $\eta$  as shown in Table 2. The improvement in  $J_{sc}$  is 36% and 38% (from 6.11 to 8.41%) in  $\eta$  for the  $TiO_2$  NPGs/xerogels based cell as compared with the P25  $TiO_2$  based one.

The photon to electron conversion efficiencies of the cells at different wavelengths can be investigated with the incident photon to charge carrier efficiency (IPCE) spectra and are shown in Figure Sb. Here, the P25  $TiO_2$  based cell exhibits the lowest efficiencies mainly because of its low dye adsorption directly resulted from its low specific surface area. For the  $TiO_2$  NPGs based cell, a clear lift in IPCE over the whole spectrum is achieved, attributable to its high specific surface area for higher dye loading and the enhanced light harvesting resulting from the submicrometer sized NPGs. The evident pick-up in IPCE at the long wavelength regime beyond 750 nm is a strong indication of the enhanced light scattering within the photoanode. After the  $TiCl_4$  treatment, the IPCE are further boosted upward because of the extra dye adsorption surface area and reduction in back electron transfer, provided by the newly generated  $TiO_2$  nanoparticles from the treatment. The incorporation of  $TiO_2$  xerogels pushes the IPCE further up and results in the highest IPCE spectrum for the  $TiO_2$  NPGs/xerogels based cell. This is due to the even more extra dye adsorption surface area, reduction in back electron transfer, and

also enhanced electron transport from the much improved inter-NPG connections offered by the  $TiO_2$  xerogels.

To analyze the characteristics of charge transfer and transport in the cell, the electrochemical impedance spectroscopy (EIS) is conducted at  $V_{oc}$  under illumination to extract the charge transfer and transport characteristics associated with the main components of the cell. For a typical DSSC, the charge transfer and transport can be modeled as a serial combination of four main components. These include the resistances accounting for the electrodes and external circuit ( $R_S$ ), the charge transfer impedance present at the counter electrode/electrolyte interface ( $R_{CE}$ ), the Nernst diffusion resistance for the electrolyte ( $R_D$ ), and the charge transport impedance accounting for the electron diffusion across the  $TiO_2$  layer and the back electron transfer reaction with the oxidized electrolyte ions at the  $TiO_2$ /dye/electrolyte interface ( $R_{TiO_2}$ ).<sup>35</sup> A typical Nyquist plot for a DSSC shows two to three arcs, with the first arc, corresponding to the high frequency region and representing  $R_{CE}$  intercepting the horizontal axis at  $R_S$ . The second arc, corresponding to the intermediate frequency region and representing  $R_{TiO_2}$ , and the third arc, corresponding to the low frequency region and representing  $R_D$ , are often too small to be observed for commonly used organic solvent based electrolytes and thin gaps between the photoanode and counter-electrode. In this work, we use acetonitrile as the electrolyte solvent and an electrode gap of 25  $\mu m$  meters. Consequently, the diffusion resistance is too small to be detected with the EIS, and the third arc is absent from the Nyquist plot shown in Figure 6.

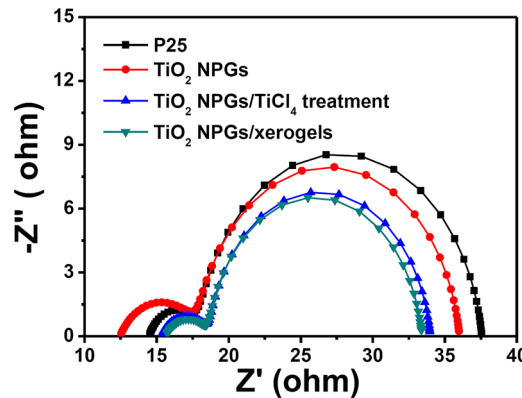


**Figure 6.** Nyquist plots of P25,  $TiO_2$  NPGs,  $TiO_2$  NPGs/ $TiCl_4$  treatment, and  $TiO_2$  NPGs/xerogels based cells under illumination.

Here, we focus on the second arc of the plot to investigate the charge transport and transfer characteristics of the photoanode. Adachi et al.<sup>35</sup> unified two different impedance models proposed by Kern et al.<sup>36</sup> and by Bisquert<sup>37</sup> for the description of electron diffusion and back electron transfer in the photoanode through a continuity equation of the conduction band/trap state electron density. There can be identified three model parameters, namely, the steady state electron density,  $n_s$ , the effective diffusion coefficient of electrons in the photoanode,  $D_{eff}$ , and the effective back electron transfer rate constants,  $k_{eff}$ . It has been noted that the electron diffusion resistance plays only a minor role in  $R_{TiO_2}$  when the cell is operated near  $V_{oc}$ .<sup>35-38</sup> Therefore, we paid attention to  $n_s$  and  $k_{eff}$ . Following the procedures detailed in Adachi et al.,<sup>35</sup>  $n_s$  and  $k_{eff}$  can be estimated from the EIS spectra, and the results are summarized in the second and third columns of Table 3. Note that  $n_s$  and  $k_{eff}$  normalized with the  $n_s$

**Table 3. Effective Electron Back Transfer Rate Constants ( $k_{\text{eff}}$ ), Steady State Electron Densities ( $n_s$ ), Electron Life Times ( $\tau_n$ ), Mean Transit Times ( $\tau_d$ ), and Electron Diffusion Coefficients ( $D_n$ ) of P25, TiO<sub>2</sub> NPGs, TiO<sub>2</sub> NPGs/TiCl<sub>4</sub> Treatment, and TiO<sub>2</sub> NPGs/Xerogels Based Photoanodes<sup>a</sup>**

	normalized $k_{\text{eff}}$	normalized $n_s$	normalized $\tau_n$	normalized $\tau_d$	normalized $D_n$
P25	1	1	1	1	1
TiO <sub>2</sub> NPGs	0.29	3.7	1.27	0.44	2.30
TiO <sub>2</sub> NPGs/TiCl <sub>4</sub>	0.29	4.4	1.61	0.32	3.11
TiO <sub>2</sub> NPGs/xerogels	0.15	8.5	2.03	0.29	3.38

<sup>a</sup>All numbers are normalized with the corresponding values of P25 based photoanode.

and  $k_{\text{eff}}$  values of P25, respectively, are presented to more clearly observe the trends among the four different photoanodes. From the data, generally, a decreasing trend in  $k_{\text{eff}}$  and an increasing trend in  $n_s$  are observed in the order of P25, TiO<sub>2</sub> NPGs, TiO<sub>2</sub> NPGs/TiCl<sub>4</sub>, and TiO<sub>2</sub> NPGs/xerogels. The indifference in  $k_{\text{eff}}$  for TiCl<sub>4</sub> treatment of TiO<sub>2</sub> NPGs is probably due to the insufficient frequency resolution around the peak region of the second arc. Note that  $k_{\text{eff}}$  is simply equal to the peak frequency of the second arc. Small  $k_{\text{eff}}$  and large  $n_s$  are desired for achieving high power conversion efficiencies. In this regard, the results for  $k_{\text{eff}}$  and  $n_s$  as determined from the EIS spectra correlate well with the trend in  $\eta$  as shown in Table 2. The increase in  $n_s$  also lifts the Fermi level of the TiO<sub>2</sub>, thus enlarging the gap between the TiO<sub>2</sub> Fermi level and the redox potential of the electrolyte to improve the  $V_{\text{oc}}$ .<sup>39</sup> Evidently, the incorporation of xerogels significantly inhibits the back electron transfer reactions and promotes creation of photoinduced electrons, in accord with the structural advantages of forming a blocking layer at the FTO–electrolyte interface, better utilization of the inter-NPG space, enhanced light harvesting, and improved structural connectivity.

In addition to EIS analysis, the electron lifetime ( $\tau_n$ ), mean transit time ( $\tau_d$ ), and electron diffusion coefficient ( $D_n$ ) in the photoanode layer are also relevant to the structural design of the photoanode and can be readily determined with the intensity-modulated photovoltage spectroscopy (IMVS) and intensity-modulated photocurrent spectroscopy (IMPS), respectively.<sup>40</sup> The results, obtained under a light intensity of 10 mW/cm<sup>2</sup>, are listed in Table 3 for comparison.

For high efficiency DSSCs, long electron life times, short transit times, and large electron diffusion coefficients are desirable. For the TiO<sub>2</sub> NPGs based photoanode, the excellent connectivity between the constituent nanocrystals provides fast electron transport pathways and leads to smaller  $\tau_d$  and larger  $D_n$  than those of the P25 based photoanode. The more effective electron transport pathways also prolong the electron lifetime by reducing the possibility of electron trapping for charge recombination. The TiCl<sub>4</sub> treatment further improves the NPGs connection at the NPGs contact region and supplies a blocking layer on top of the substrate, both benefiting the electron transport and reduction in charge recombination. Consequently, the  $\tau_d$  is further reduced and  $\tau_n$  and  $D_n$  are further increased. As for the TiO<sub>2</sub> NPGs/xerogels composite based photoanode, the xerogels offer even better inter-NPG connections than the TiCl<sub>4</sub> treatment does, not just at the NPGs contact region but across the whole inter-NPG space. With this, the lowest  $\tau_d$  and the highest  $\tau_n$  and  $D_n$  are achieved, leading to the drastic improvement in the power conversion efficiency.

## 4. CONCLUSION

A facile one-step hydrothermal process is developed to prepare mesoporous TiO<sub>2</sub> NPGs of high specific surface areas and adequate pore sizes for applications in DSSCs as the photoanode material. The process uses a metal salt as the precursor. Through a parametric study on two key reaction parameters, the molar concentration of the Ti source and the molar concentration ratio of the etching ion versus the Ti source, product NPGs with an optimum combination of the specific surface area (166 m<sup>2</sup>/g) and average pore size (8.9 nm) are obtained. A new form of composite photoanode is proposed and is composed of mesoporous TiO<sub>2</sub> NPGs/xerogels. This composite photoanode possesses several structural advantages beneficial for boosting the power conversion efficiencies of the DSSCs, including the effective utilization of the inter-NPG space with the infiltration of the xerogels, the excellent structural connectivity within and across the NPG and xerogel domains for fast electron transport, the high specific surface areas of both the NPGs and the xerogels for providing abundant dye adsorption for generation of photoinduced electrons, the formation of a TiO<sub>2</sub> xerogel blocking layer on top of the substrate to inhibit the back electron transfer reaction, and the submicrometer size of the NPGs to improve the light harvesting efficiency. A drastic power conversion efficiency boost of 38% is achieved with the present composite photoanode based cell as compared with a P25 TiO<sub>2</sub> based one.

## ■ AUTHOR INFORMATION

### Corresponding Author

\*E-mail: sylu@mx.nthu.edu.tw.

### Notes

The authors declare no competing financial interest.

## ■ ACKNOWLEDGMENTS

This work was financially supported by the National Science Council of the Republic of China (Taiwan) under Grants NSC-98-2221-E-036-MY3 and NSC-98-3114-E-007-005 and by the Low Carbon Energy Research Center of the National Tsing-Hua University.

## ■ REFERENCES

- O'Regan, B.; Grätzel, M. *Nature* **1991**, *353*, 737.
- Nazeeruddin, M. K.; Kay, A.; Rodicio, I.; Humphry-Baker, R.; Muller, E.; Liska, P.; Vlachopoulos, N.; Grätzel, M. *J. Am. Chem. Soc.* **1993**, *115*, 6382.
- Grätzel, M. *Nature* **2001**, *414*, 338.
- Palomares, E.; Clifford, J. N.; Haque, S. A.; Lutz, T.; Durrant, J. R. *J. Am. Chem. Soc.* **2003**, *125*, 475–482.
- Hu, L. H.; Dai, S. Y.; Wen, J.; Xiao, S. F.; Sui, S. F.; Huang, Y.; Chen, S.; Kong, F.; Pan, X.; Liang, L.; Wang, K. *J. Phys. Chem. B* **2007**, *111*, 358.
- Kuo, C.-Y.; Lu, S.-Y. *Nanotechnology* **2008**, *19*, 095705.

- (7) Tsai, T.-Y.; Lu, S.-Y. *Electrochem. Commun.* **2009**, *11*, 2180.  
(8) Hsiao, C.-T.; Lu, S.-Y.; Tsai, T.-Y. *Chem.—Eur. J.* **2011**, *17*, 1358.  
(9) Ku, S.-Y.; Lu, S.-Y. *Int. J. Electrochem. Sci.* **2011**, *6*, 5219.  
(10) Tsai, T.-Y.; Lu, S.-Y. *J. Electrochem. Soc.* **2011**, *158*, B1306.  
(11) Hagfeldt, A.; Grätzel, M. *Chem. Rev.* **1995**, *95*, 49.  
(12) Liu, B.; Aydil, E. S. *J. Am. Chem. Soc.* **2009**, *131*, 3985.  
(13) Krishnamoorthy, T.; Thavasi, V.; Subodh, M.; Ramakrishna, S. *Energy Environ. Sci.* **2011**, *4*, 2807.  
(14) Jiu, J.; Isoda, S.; Wang, F.; Adachi, M. *J. Phys. Chem. B* **2006**, *110*, 2087.  
(15) Kang, S. H.; Choi, S. H.; Kang, M. S.; Kim, J. Y.; Kim, H. S.; Hyeon, T.; Sung, Y. E. *Adv. Mater.* **2008**, *20*, 54.  
(16) Myahkostupov, M.; Zamkov, M.; Castellano, F. N. *Energy Environ. Sci.* **2011**, *4*, 998.  
(17) Mor, G. K.; Shankar, K.; Paulose, M.; Varghese, O. K.; Grimes, C. A. *Nano Lett.* **2006**, *6*, 215.  
(18) Yoon, J.-H.; Jang, S.-R.; Vittal, R.; Lee, J.; Kim, K.-J. *J. Photochem. Photobiol., A* **2006**, *180*, 184.  
(19) Hore, S.; Vetter, C.; Kern, R.; Smit, H.; Hinsch, A. *Sol. Energy Mater. Sol. Cells* **2006**, *90*, 1176.  
(20) Shao, W.; Gu, F.; Li, C.; Lu, M. *Inorg. Chem.* **2010**, *49*, 5453.  
(21) Zhang, Q.; Park, K.; Xi, J.; Myers, D.; Cao, G. *Adv. Energy Mater.* **2011**, *1*, 988.  
(22) Dürr, M.; Schmid, A.; Obermaier, M.; Rosselli, S.; Yasuda, A.; Nelles, G. *Nat. Mater.* **2005**, *4*, 607.  
(23) Tan, B.; Wu, Y. *J. Phys. Chem. B* **2006**, *110*, 15932.  
(24) Chen, D.; Huang, F.; Cheng, Y. B.; Caruso, R. A. *Adv. Mater.* **2009**, *21*, 2206.  
(25) Kim, Y. J.; Lee, M. H.; Kim, H. J.; Lim, G.; Choi, Y. S.; Park, N. G.; Kim, K.; Lee, W. I. *Adv. Mater.* **2009**, *21*, 3668.  
(26) Chou, T. P.; Zhang, Q.; Fryxell, G. E.; Cao, G. *Adv. Mater.* **2007**, *19*, 2588.  
(27) Maldonado-Hódar, F. J.; Moreno-Castilla, C.; Rivera-Utrilla, J. *Appl. Catal., A* **2000**, *203*, 151.  
(28) Boujday, S.; Wünsch, F.; Portes, P.; Bocquet, J.-F.; Colbeau-Justin, C. *Sol. Energy Mater. Sol. Cells* **2004**, *83*, 421.  
(29) Ischia, M.; Campostrini, R.; Lutterotti, L.; García-López, E.; Palmisano, L.; Schiavello, M.; Pirillo, F.; Molinari, R. *J. Sol-Gel Sci. Technol.* **2005**, *33*, 201.  
(30) Sauvage, F.; Chen, D.; Comte, P.; Huang, F.; Heiniger, L. P.; Cheng, Y. B.; Caruso, R. A.; Grätzel, M. *ACS Nano* **2010**, *4*, 4420.  
(31) Huang, F.; Chen, D.; Zhang, X. L.; Caruso, R. A.; Cheng, Y. B. *Adv. Funct. Mater.* **2010**, *20*, 1301.  
(32) Yu, I. G.; Kim, Y. J.; Kim, H. J.; Lee, C.; Lee, W. I. *J. Mater. Chem.* **2011**, *21*, 532.  
(33) Zhang, Q.; Cao, G. *J. Mater. Chem.* **2011**, *21*, 6769.  
(34) Roy, P.; Kim, D.; Paramasivam, I.; Schmuki, P. *Electrochem. Commun.* **2009**, *11*, 1001.  
(35) Adachi, M.; Sakamoto, M.; Jiu, J.; Ogata, Y.; Isoda, S. *J. Phys. Chem. B* **2006**, *110*, 13872.  
(36) Kern, R.; Sastrawan, R.; Ferber, J.; Stangl, R.; Luther, J. *Electrochim. Acta* **2002**, *47*, 4213.  
(37) Bisquert, J. *J. Phys. Chem. B* **2002**, *106*, 325.  
(38) Murakami, T. N.; Ito, S.; Wang, Q.; Nazeeruddin, M. K.; Bessho, T.; Cesar, I.; Liska, P.; Humphry-Baker, R.; Comte, P.; Pechy, P.; Gratzel, M. *J. Electrochem. Soc.* **2006**, *153*, A2255.  
(39) Gajjela, S. R.; Ananthanarayanan, K.; Yap, C.; Gratzel, M.; Balaya, P. *Energy Environ. Sci.* **2010**, *3*, 838.  
(40) Pan, K.; Dong, Y.; Tian, C.; Zhou, W.; Tian, G.; Zhao, B.; Fu, H. *Electrochim. Acta* **2009**, *54*, 7350.